

The Role of Grain Boundaries on Ionic Defect Migration in Metal Halide Perovskites

Nga Phung, Amran Al-Ashouri, Simone Meloni, Alessandro Mattoni, Steve Albrecht, Eva L. Unger, Aboma Merdasa,* and Antonio Abate*

Halide perovskites are emerging as revolutionary materials for optoelectronics. Their ionic nature and the presence of mobile ionic defects within the crystal structure have a dramatic influence on the operation of thin-film devices such as solar cells, light-emitting diodes, and transistors. Thin films are often polycrystalline and it is still under debate how grain boundaries affect the migration of ions and corresponding ionic defects. Laser excitation during photoluminescence (PL) microscopy experiments leads to formation and subsequent migration of ionic defects, which affects the dynamics of charge carrier recombination. From the microscopic observation of lateral PL distribution, the change in the distribution of ionic defects over time can be inferred. Resolving the PL dynamics in time and space of single crystals and thin films with different grain sizes thus, provides crucial information about the influence of grain boundaries on the ionic defect movement. In conjunction with experimental observations, atomistic simulations show that defects are trapped at the grain boundaries, thus inhibiting their diffusion. Hence, with this study, a comprehensive picture highlighting a fundamental property of the material is provided while also setting a theoretical framework in which the interaction between grain boundaries and ionic defect migration can be understood.

1. Introduction

Halide perovskites have rapidly become an attractive class of materials for optoelectronic applications, including photovoltaics,^[1] light-emitting diodes (LEDs),^[2] light detection,^[3] and energy storage.^[4] The stoichiometric unit of a halide perovskite with standard formula ABX_3 consists of either one organic or inorganic monovalent ion (A^+) placed in a cage made up of eight corner-sharing octahedra, each containing one divalent metal ion (B^{2+}) (typically Pb or Sn), and six halides (X^-). All three ionic constituents may give rise to defects in the form of vacancies, interstitials, or antisite substitutions.^[5] Ionic defects have been shown to be very mobile at room temperature,^[6] being able to migrate within the material (lattice) when subjected to temperature or defect concentration gradients, as well as external stimuli such as light or an electric field.^[7,8] As this gives rise to substantial transient

N. Phung, A. Al-Ashouri, Prof. S. Albrecht, Dr. E. Unger, Dr. A. Merdasa, Dr. A. Abate
Helmholtz-Zentrum Berlin
Kekuléstr. 5, Berlin D-12489, Germany
E-mail: aboma.merdasa@helmholtz-berlin.de, aboma.merdasa@forbrf.lth.se; antonio.abate@helmholtz-berlin.de, antonio.abate@unina.it

Dr. S. Meloni
Dipartimento di Scienze Chimiche e Farmaceutiche (DipSCF)
Università degli Studi di Ferrara (Unife)
Via Luigi Borsari 46, Ferrara I-44121, Italy


Dr. A. Mattoni
Consiglio Nazionale delle Ricerche
Istituto Officina dei Materiali
CNR-IOM, Cagliari
Cittadella Universitaria
Monserato CA 09042-I, Italy

Prof. S. Albrecht
Faculty of Electrical Engineering and Computer Science
Technical University Berlin
Marchstraße 23, Berlin 10587, Germany

Dr. E. L. Unger
Department of Chemistry and NanoLund
Lund University
Naturvetarvägen 14, Lund 22362, Sweden

Dr. A. Merdasa
Department of Physics
Lund University
Sölvegatan 14, Lund 22362, Sweden

Dr. A. Abate
Department of Chemical
Materials and Production Engineering
University of Naples Federico II
Piazzale Tecchio 80, Fuorigrotta, Naples 80125, Italy

 The ORCID identification number(s) for the author(s) of this article can be found under <https://doi.org/10.1002/aenm.201903735>.

© 2020 Helmholtz Zentrum Berlin (HZB). Published by WILEY-VCH Verlag GmbH & Co. KGaA, Weinheim. This is an open access article under the terms of the Creative Commons Attribution License, which permits use, distribution and reproduction in any medium, provided the original work is properly cited.

DOI: 10.1002/aenm.201903735

phenomena in the electrical response of a device, a considerable portion of the literature to date discusses the challenges arising from ionic defects created during device operation and their migration. Not only does ionic migration play a crucial role in the device's current–voltage hysteresis,^[9,10] but is also attributed the underpinning cause for both reversible and irreversible degradation of the perovskite absorber.^[11,12] Since ionic defect formation, and consequent ionic defect movement, are evidently an integral part of the operation and stability of perovskite-based optoelectronic devices, it is imperative to continue gaining an understanding of the migration dynamics.

Ion migration relates closely to the defect chemistry of the material.^[13] Theoretical calculations^[13,14] and experimental work^[15] support the hypothesis that the most abundant defects in methylammonium lead iodide (MAPbI₃) perovskites are iodide vacancies (V_I[•]) and interstitials (I_I[']) as these have the lowest formation energies and are likely generated as Frenkel pairs. Ionic defect migration has been proposed to occur via efficient vacancy hopping or interstitial kick-off mechanisms.^[10] One of the leading questions of the experiments presented here is the effect of grain boundaries (GBs) on ionic migration in polycrystalline films, as these cause a discontinuation of the crystal lattice with substantial defect density. This is of particular relevance for solution-processed perovskite thin films, which typically contain a large number of GBs.

The exact interplay of GBs and ionic motion is still under discussion in the literature. Some suggest that ionic defect migration could be facilitated by GBs,^[16,17] which is based on observations of a more considerable hysteresis at the GBs compared to the grain interior, as concluded by atomic force microscopy experiments.^[16] Moreover, the activation energies for ions to migrate from their proper places in the lattice are reportedly higher in single crystals compared to thin films with smaller grains (≈300 nm).^[18] This may be due to the increased difficulty for ions to move in the absence of GBs because of the lack of ionic vacancies. On the other hand, others and some of us have observed a reduction in hysteresis for devices containing an absorber layer with larger grain size.^[19,20] It was concluded from intensity-modulated photocurrent spectroscopy that ionic defect movement is faster when the number of GBs is reduced,^[19] which points to GBs inhibiting their migration. Another recent report has shown that even though mobile ions is a prerequisite for hysteresis, the trapping and detrapping of ionic defects plays an important role for slow transients seen in devices.^[21]

To extend our understanding about how the microstructure influences ionic defect migration, we recognize the need for direct observations of the migration dynamics and for gaining a spatially resolved microscopic picture. Photoluminescence (PL) microscopy offers the opportunity to study the light absorber material while excluding the influence of other contact layers or metal electrodes that are typically used in optoelectronic devices. Hence, PL microscopy has particularly been used to detect the effect of defect migration in halide perovskites.^[8,22,23] One characteristic signature is the change in relative PL quantum yield, which is directly related to the rate of radiative versus nonradiative recombination, which in turn is dictated by the local defect chemistry (and density), which can be altered by light.^[24,25] It has been widely reported that light can drive out the iodide content and change the PL yield, or in other words, iodide defects have

been shown to alter the PL yield in halide perovskites.^[22,26,27] With PL microscopy we can induce local defect formation and migration while to some extent resolving the microstructure of the material, thus allowing us to correlate the dynamics of defect diffusion to the presence or absence of GBs.

In this study, PL microscopy is used as a means to induce ionic defect migration with the excitation beam, consecutively track the motion (redistribution) of defects in real-time through the resulting fluctuation in PL intensity, and observe the extent to which the material recovers from the limited perturbation state. We opted to use MAPbI₃ to limit the possible combinations of constituent ions and their associated defects. We observe changes in the PL signal with subsecond time resolution (50 ms), which allows us to directly resolve defect-induced changes in the optoelectronic properties of the material relating to ionic motion. By correlating PL microscopy and energy dispersive X-ray spectroscopy (EDX), we confirm that light promotes ionic diffusion out of the excited spot, creating additional defects in the material. By monitoring the dynamics of the relative PL quantum yield over time and space in MAPbI₃ crystals and films of different grain sizes, we can investigate the impact of GBs on the defect migration. With the support of atomistic simulations, we conclude that the GBs inhibit the lateral movement of defects in the material, i.e., their spreading across the sample, which we also demonstrate with devices comprised of perovskite absorbers of different grain sizes. Here we show that devices are required to have monolithic grains in order to have fast ionic response. The fast transient response in the device can potentially reduce the reversible losses due to slow ion migration seen in devices under operational conditions.^[11] Our study gives a broader understanding of how ionic defect migration in halide perovskite relates to the microstructure of the material.

2. Results and Discussion

2.1. Photoinduced Ion Migration

To establish the link between PL yield and defect migration, we expose a MAPbI₃ thin film fabricated by a solution-based one-step method^[28] (see the Experimental Section for more details) to 1 min of continuous wave laser excitation (450 nm). After exposure with focused excitation, we switch to a wide-field excitation to obtain a PL map and observe that the region exposed to the focused laser has a significantly reduced PL yield (**Figure 1a**). From the scanning electron microscope (SEM) micrograph of the same area **Figure 1b₁**, it appears as if the region has structurally collapsed to form what resembles a crater. Furthermore, it becomes evident from the EDX images (**Figure 1b_{2–4}**) that there is a significant ionic redistribution. Most obvious is the almost complete lack of iodide (**Figure 1b₂**), which is in agreement with previous reports on halide migration away from the light exposed spot.^[22,26,27] There is also no indication that it has accumulated elsewhere, although it is possible that the EDX image resolution prevents a clear representation of the elemental distribution outside the illuminated region. **Figure 1b₃** shows a slight reduction of the C signal after laser excitation, which could imply a removal of the methylammonium cation (CH₃NH₃⁺) due to laser excitation. The signal for Pb, on the other hand,

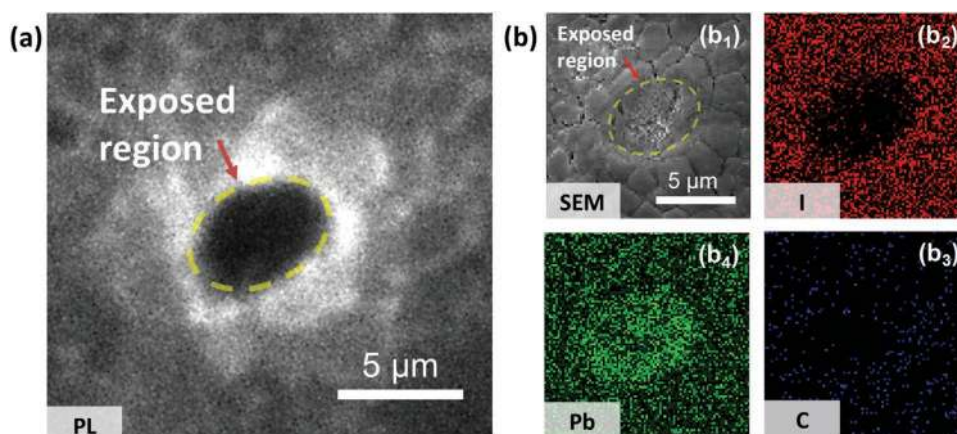


Figure 1. a) Photoluminescence wide-field image directly after 1 min of focused laser exposure in a MAPbI₃ thin film. b) Scanning electron microscopic (SEM) (panel b₁) and energy dispersive X-ray (EDX) images representing elemental distribution of the elements I, C, and Pb (panels b₂, b₃, b₄, respectively), recorded from the same film area 45 min after laser exposure.

is higher in the exposed region compared to the surrounding regions (Figure 1b₄). At first this may seem counter-intuitive, however consistent with the EDX images of I and C, the increase of the Pb signal just denotes an increase of the concentration of Pb with respect to the other elements, I and C. Whether this is due to the concomitant formation of I₂ and Pb⁰[29] or collapse of the tetragonal structure into PbI₂ due to the removal of MA⁺ and I⁻,[30] goes beyond the aim of this work. Indeed, the reduced concentration of I and C in the illuminated region can further enhance the Pb signal in EDX imaging because it reduces the reabsorption of Pb-emitted X-rays by MA⁺ and I⁻.

Most importantly, this correlation between PL and EDX allows us to establish that ion (re)distribution can be driven either directly or indirectly (via thermal effects) by light and it correlates strongly to the changes in PL quantum yield. A reduction of PL yield correlated with a depletion of iodine can be rationalized by migrating ions increasing the defect concentration, which consequently increases the portion of nonradiative recombination. As also reported in several publications,[22,26,27] we suspect that it is the halide specie having the lowest activation energy, which migrates out from the laser excited spot forming the defects. A recent report by Motti et al. shows that a reduction in PL yield after light soaking relates to an increment in the halide interstitial concentration which can trap holes.[31] Moreover, the formation of metallic Pb has been shown to introduce deep traps in the bandgap of MAPbI₃ introducing nonradiative recombination centers.[32] It is also worth noting that the reduction of C signal in EDX might be related to formation of MA⁺ vacancies which are known to diffuse slowly under light exposure.[33] Identifying the type of point defects generated and set in motion by intense light exposure requires additional measurements stretching out of the scope of this work and is therefore the focus of a follow up study.

2.2. Tracking Ion Migration via Spatially Resolved Photoluminescence

To further understand the effect of microstructure on the ion migration, we compare MAPbI₃ samples in form of

polycrystalline thin films of different grain sizes and a crystal grown by inverted crystallization[34] (fabrication details are given in the Experimental Section). Having established that we can induce ionic defect migration with a focused laser beam, we subject the samples to a measurement protocol in which the excitation beam is either focused into a spot (full width at half maximum, FWHM, of 2.5 μm) in the center of the field of view, or spread across the entire field of view spanning an area up to 40 μm diameter (defocused). A detailed description of the experimental setup and measurement protocol can be found in Note S1 (Supporting Information).

Figure 2a schematically illustrates the two modes also showing the corresponding excitation spot sizes. In both excitation modes, the excitation power is kept constant, which means the excitation density in the focused mode increases by over two orders of magnitude compared to the defocused mode. Irrespective of whether the excitation is focused or defocused, the PL emission from the sample is collected from the entire field of view (40 μm diameter) of the sample at a frame rate of 20 Hz. This provides a unique opportunity to not only detect the spatially evolving PL signal from the area of the sample which is not directly excited in the focused mode, but also detect any changes in the PL as a result of focusing the laser (comparing defocused PL images before (PL₀) and after focusing the laser (PL₁)—see inset of Figure 2d–e).

Figure 2b,c shows a spatially resolved time evolution of PL from the thin film and a freshly cleaved surface of the crystal in the focused mode excitation interval (a few selected frames over 6 s, see Video S1 for the thin film and Video S2 for the crystal). Since the redistribution of PL is radially symmetric with respect to the point of excitation, we plot the normalized PL intensity as a function of the distance d from the center of the laser spot ($d = 0 \mu\text{m}$). The radial distribution of PL intensity extracted at each time instant ($\text{PL}(d,t)$) is normalized to the initial PL distribution ($\text{PL}(d,t = 0)$) measured just as the focused excitation is turned on. For both samples, a reduction of the normalized PL (values below the red dotted line) is observed for $d < \approx 2 \mu\text{m}$. We note that this correlates well with the region where the focused excitation laser directly strikes the sample (blue line). Overall, the PL signal of the film and crystal shows relevant qualitative

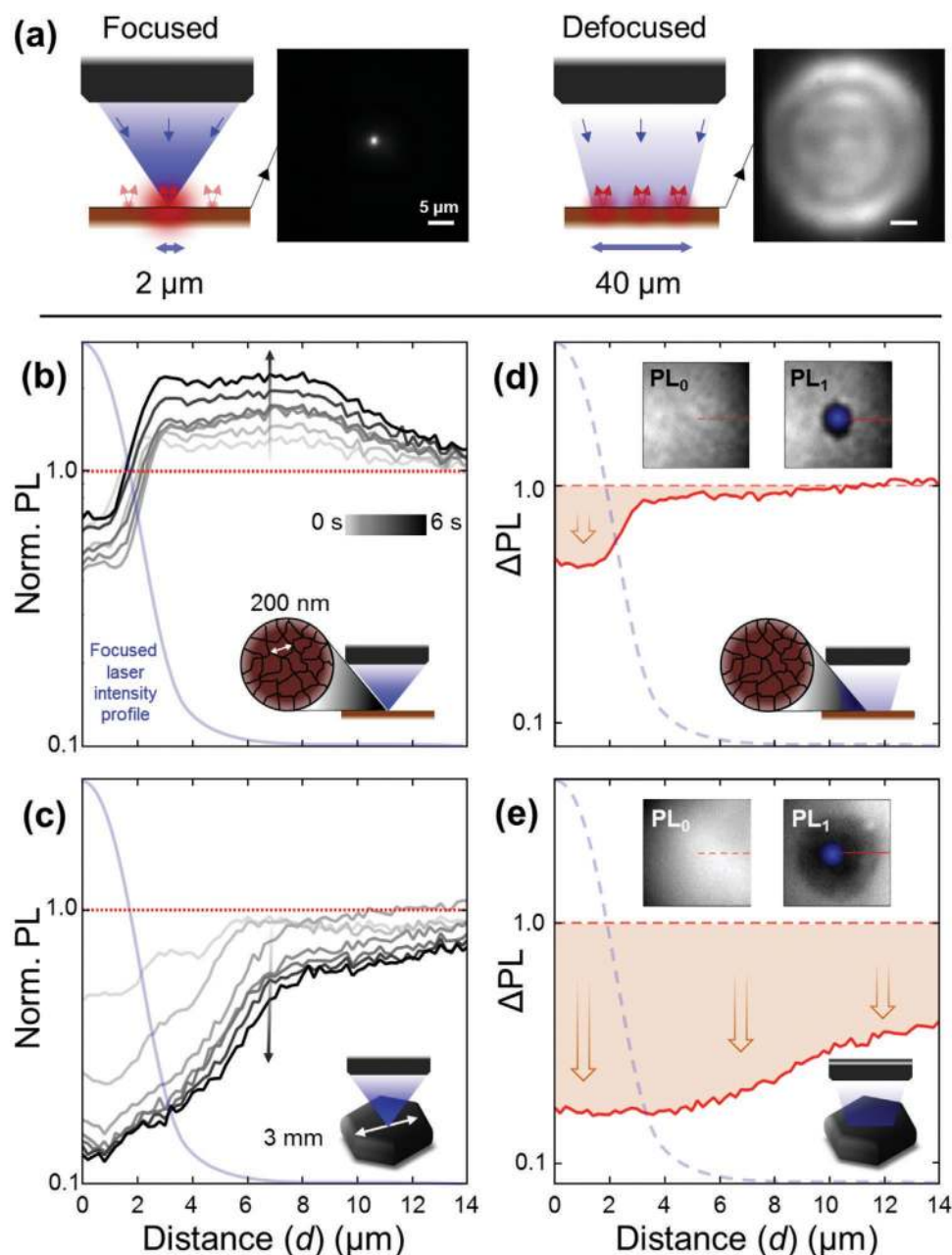


Figure 2. a) The excitation modes used in this study: a focused mode where the excitation area has a diameter of 2.5 μm and a defocused mode where the excitation area has a diameter of 40 μm . PL images of fluorescent highlighter ink on a glass substrate demonstrating the excitation area for each mode (scale bar represents 5 μm in both images). Irrespective of the excitation mode used, photoluminescence (PL) signals from samples are collected from the entire field of view. The evolution of normalized PL during the first 6 s of exposure to the focused excitation of the b) thin film and c) crystal as a function of radial distance, d , from the center of focused laser excitation spot. The gray-scale bar in panel (b) indicates the elapsed time after which the traces in (b) and (c) are extracted. The light-blue curve shows the normalized laser intensity profile when the light is focused, also indicated in the insets as blue spots. Spatially resolved changes in PL intensity (ΔPL) are shown in (d) for a thin film and in (e) for a crystal comparing the distribution of PL before and after the focused excitation. The red shaded area represents the amount PL has dropped. The top two insets in panel (d) and (e) show the PL images with defocused excitation before and after a 20 s period of focused excitation. The schematic insets in panels (b)–(e) indicate the sample and excitation mode used.

differences both in the shape and variation with time. In the crystal, the PL diminishes over a broad range (broader than the excitation spot) upon excitation with the focused beam. On the contrary, PL in the film decreases only in the laser spot; outside this region PL increases. Moreover, while for the crystal

$\text{PL}(d,t)$ keeps decreasing with time during the first 6 s of the measurement, in the film $\text{PL}(d,t)$ continuously increases.

An interesting feature for both samples is that PL is detected at distances far from the excitation point. Charge carrier diffusion lengths in metal halide perovskites have been

reported to be on the order of a few μm ,^[35,36] which may certainly explain our observations. Another contributing factor may also be photon recycling.^[37] We are reluctant to attribute this to PL caused by direct absorption of photons from the tail of the focused excitation source primarily for the reason that the PL profiles for neither sample (gray traces) resemble that of the focused excitation profile (blue traces). Regardless of how the PL far from the focused excitation spot is generated, it is more importantly established that there are changes in the spatially distributed PL yield evolving over seconds (slow time scale), which we attribute to ionic defect redistribution. This is in agreement with a study by Li et al.,^[23] in which PL changes are also observed in space in a MAPbI₃ thin film due to an applied electric field-induced ionic redistribution.

Although we have strong evidence for light inducing ionic redistribution, we refrain from proposing by which mechanism this occurs at this stage. In a recent report, light-driven ion migration has been attributed to photochemical processes involving various rates of trapping and detrapping of charge carriers interacting with halide defects.^[38] Alternatively, it has been also proposed that light can induce local electric fields causing ionic defect migration, although different explanations of how that field arises have been proposed including photo-induced Stark effect,^[39] as well as an interaction between charge carriers and surface adhered superoxide species.^[40]

The comparison between the PL images before (PL₀) and after (PL₁) focusing the excitation can provide information on lasting changes (in minutes or hours) in the spatially distributed PL intensity caused by the focused excitation. For a simplified comparison between samples, we extract the relative change in PL intensity $\Delta\text{PL}(d) = \frac{\text{PL}_1(d)}{\text{PL}_0(d)}$, again as a function of radial distance (d). In Figure 2d, we demonstrate that ΔPL shows a significant reduction in the range between $d = 1$ and $4 \mu\text{m}$ (red shaded area) for the thin film. Comparing this to the FWHM of the focused laser distribution profile (blue traces), this reduction of PL coincides with the region receiving the direct excitation from the focused laser. The insets show the PL images before and after the focused excitation where the PL reduction is observed. A value of $\Delta\text{PL} < 1$ indicates an increase of defect-mediated nonradiative recombination, which is associated with a redistribution of ions and subsequent defect formation as discussed above. Subjecting the freshly cleaved crystal to the same measurement procedure results in a noticeably larger reduction of ΔPL observed at a greater radial distance compared to the thin film (Figure 2e), which is also evident in the PL images (see insets in Figure 2e). At a radial distance of $d = 12 \mu\text{m}$, $\Delta\text{PL} = 1$ for the thin film (no lasting effect from focused excitation), as opposed to the crystal case, where $\Delta\text{PL} \approx 0.3$. We, therefore, conclude that there is stronger resistance to the spatial redistribution of ionic defects in the thin film compared to the crystal.

2.3. Grain Boundaries as an Energy Barrier for Ion Migration

As shown in Figure S2a (Supporting Information), the average grain size of the thin film shown in Figure 2 is $\approx 200 \text{ nm}$, which is approximately one order of magnitude smaller than the diameter of the focused excitation spot ($\approx 2.5 \mu\text{m}$). Therefore,

the laser spot directly impinges on an area containing several grains, which is not the case for the crystal (see Figure S2b in the Supporting Information). Hence, we prepare a thin film containing large grains, which serves as an intermediate scenario between the small grain thin film and the single crystal. SEM micrograph demonstrates that this “big-grain film” has grains with sizes equivalent to, or even larger than, the focused laser excitation spot (see Figure S2c in the Supporting Information). As such, we can focus the excitation into a single grain while observing the effect on the neighboring grains that are not directly excited. Here, we depend on SEM micrographs to define the size of the grains. We acknowledge that these can vary from what is determined by SEM,^[41] and that a group of grains can be mistaken for a single one using this technique.^[42] However, this study emphasizes the difference in the GB density in the three samples with notably different microstructure (further optical and morphological characterization of the samples can be found in Notes S2 and S3 in the Supporting Information). Hence, we are confident that adequate information can still be drawn from relative differences between SEM analyses.

In Figure 3, we isolated a relatively large grain ($\approx 5 \mu\text{m}$ diameter) and subjected it to the same measurement procedure as for the thin film and crystal. We did not correlate SEM micrographs with PL measurements but could identify the grain boundaries in the PL microscope as regions of particularly increasing PL intensity for the first 30 s of exposure to light. This photobrightening at GBs can be explained by an intense light-induced healing of defects,^[43] that, in comparison to the bulk of the grain where the defect density is lower, occurs at a faster rate. In Figure 3a, the PL map is shown in defocused mode (PL₀) prior to focusing the excitation, where the large grain is highlighted with a dashed yellow line. When the excitation is focused into the grain (blue spot), we observe from the normalized PL images that emission is coming strictly from the grain that is directly excited (Figure 3b) and not from outside its GB. This points to GBs either efficiently mediating nonradiative recombination or that charge carriers are simply deflected, which has been previously proposed.^[5,44] As the focused excitation remains, we observe similar spatial redistribution of PL to what occurs in the single crystal (see Video S3 in the Supporting Information), establishing the light-induced ionic defect migration. As the excitation is switched back to defocused mode (PL₁), we can confirm that PL remains significantly reduced exclusively for the grain that is excited (Figure 3c). This becomes more obvious in Figure 3d when plotting ΔPL from a cross-section of the field of view (indicated by the red line in Figure 3c), where not only a strong reduction of PL is observed for the excited grain, but also that PL remains largely unaffected outside the boundaries of the large grain. Thus, this intermediate case strengthens the hypothesis that GBs introduce barriers for ion migration.

We further fabricated devices in n-i-p architecture using thin films of different grain sizes to examine the effect of ionic defect dynamics in working solar cells. Figure 3e shows the current density–voltage curves of devices employing two distinct grain size distributions, in which the “big grain” device has average absorber grain size of 400 nm compared to an average grain size of 200 nm for the “small grain” device. The devices have fairly similar performance where the small-grain and

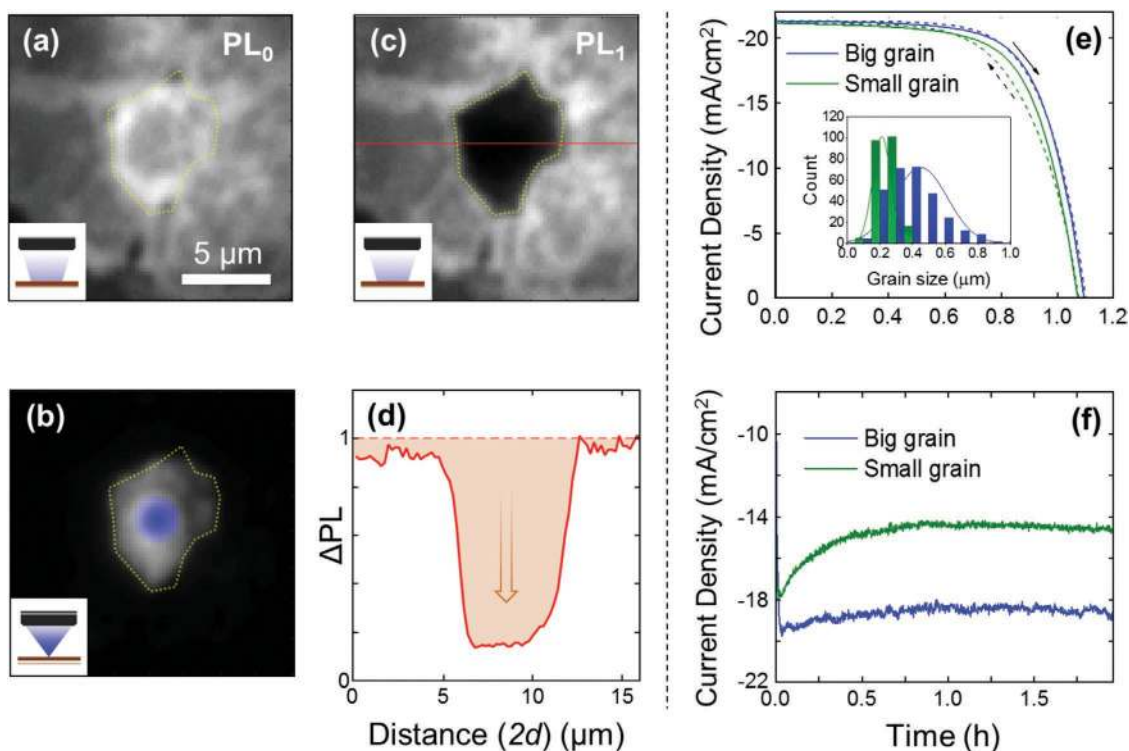


Figure 3. The evolution of the PL signal during focused mode excitation on a big grain film. a) Initial defocused mode PL_0 , b) focused mode snapshot in which the laser excitation spot is indicated by a blue circle. c) PL at defocused excitation mode (PL_1). d) Relative change ΔPL as a function of distance along the red line in (c). The device behavior employing different grain sizes: e) current density–voltage curves of the devices measured under AM 1.5 solar simulator with scan rate of 100 mV s^{-1} , arrows indicate scan direction (inset shows the grain size distributions of identical perovskite films) and f) current response at 0.1 V bias for 2 h of corresponding devices under one Sun illumination.

big-grain devices show short circuit current density of 21.1 and 21.3 mA cm^{-2} , open circuit voltage of 1074 and 1095 mV, and fill factor of 66.4% and 68.0% respectively (forward scan), resulting in 15.0% and 15.8% power conversion efficiencies. The small-grain device exhibits a slight hysteresis compared to the big-grain device which might indicate a difference in the ionic response time. Furthermore, the devices were subjected to 0.1 V bias to track the current transient behavior under illumination (Figure 3f). As expected, the big grain device has a faster current response with less variance under a steady bias. Thus, in agreement with a previous report by Correa-Baena et al.,^[19] the microstructure of the film can be linked to the device's behavior, in which the electronic transient on long time scales has been attributed to the ionic double layers introduced by ionic defect migration.^[11,45]

2.4. Dark Recovery

Having established that the light-induced ion migration is inhibited by GBs, we study the effect of allowing the sample to rest in the dark after light soaking, which has for PSC devices been reported to restore performance.^[11] For both the crystal and the big-grain film, where a noticeable ion migration is detected over large areas, we observe the self-healing (recovery of PL) occurring at different time scales (Figure 4a) which is also observed by several reports,^[27,46,47] and is attributed to

ionic defect migration.^[48] The main difference in the recovery between the two samples here are the time scales and the extent to which recovery occurs (Figure 4b). Complete recovery occurs for the crystal within 1 h, while the recovery for the big-grain film is still incomplete after 12 h. We note that for the big-grain film, recovery starts from the GB perimeter and progresses to the center of the grain, where the PL yield remains low even after 12 h. The longer recovery time seen along the perimeter of the grain might be due to either a higher intrinsic defect concentration and/or an intragrain microstructure evolution constraint, which prevents the restoration of the initial state. We propose that the ions that have been driven toward, and possibly accumulated or “kinetically trapped” at the GBs, can return and “heal” only the damaged part in its proximity.

It is important to note here that we observe a morphology change in the big grain film (Figure S3, Supporting Information) and similarly in the small grain film (Figure 1) after the light exposure. More importantly, the fact that the PL yield can recover implies that constituent ions did not leave the samples after excitation, but rather redistribute in the sample. We attribute the recovery to ionic defect annihilation, which leads to a reduction of nonradiative recombination, and thus, recovery of PL yield.

Atomistic simulations support the hypothesized scenario. Classical molecular dynamics (MD) makes it possible to simulate large-scale models of MAPbI_3 including point-defects and GBs. Interatomic forces of MAPbI_3 can be modeled by the MYP

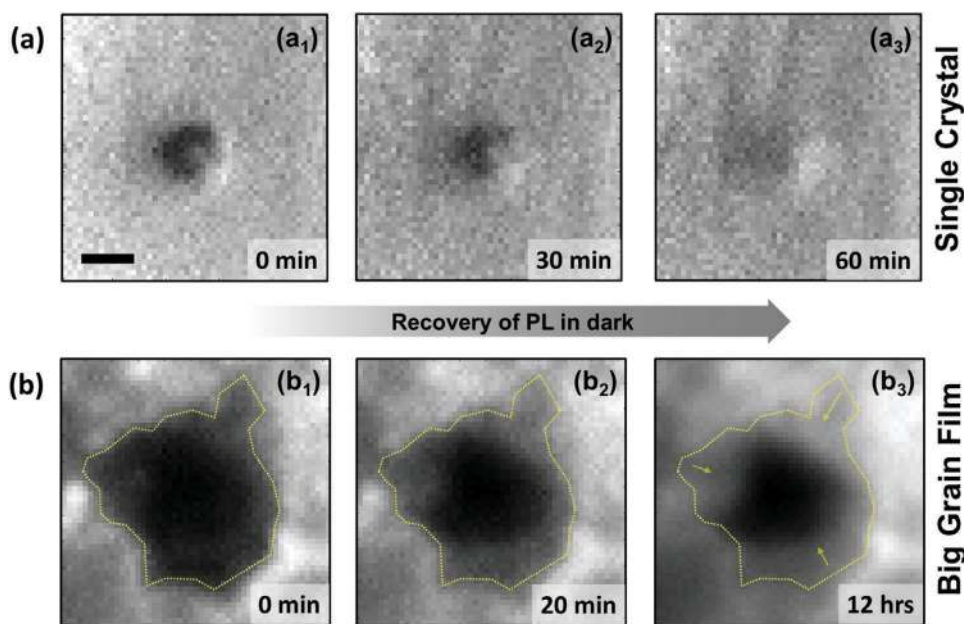


Figure 4. The PL images demonstrating the recovery of PL in dark over time for a) single crystal, and b) big-grain film (yellow dotted line indicates the boundary of one single grain). Light is only switched on for the time required to acquire the image (<1 s). The time-stamp in the bottom right corner indicates the time after which focused light-soaking finished and recovery began. For the single crystal there is nearly a complete recovery of PL within 60 min in dark, whereas for the big-grain film the recovery is only partial after 12 h. Scale bar represents 2 μm in all images.

force field developed by Mattoni et al.^[49,50] which have been successfully applied to study vibrations and thermodynamic properties of MAPbI_3 , degradation in water^[51,52] as well as diffusion of point-defects.^[6] Here, we apply MD to simulate the diffusion of one iodine vacancy (i.e., the most mobile point defect in MAPbI_3 ^[6]) in presence of the $\Sigma 5/(102)$ grain boundary, i.e., a prototypical boundary in MAPbI_3 forming along the (102) crystallographic plane with 53.1° tilt angle.^[53] The calculated dynamics shows that the mobility of the iodine vacancy is strongly reduced

by the presence of boundaries. **Figure 5a** shows the position-time plot of the vacancy position within a grain. The trajectory within the atomistic model is also represented in **Figure 5b**. The vacancy is initially placed at the center of a crystal grain annealed at 400 K for 0.5 ns. We chose this temperature due to higher diffusivity of ions at higher temperature. Note that the diffusion mechanism is unchanged between 400 and 300 K, whereas higher temperature shortens the simulation time. When the defect is far from the boundary, it diffuses randomly through stochastic

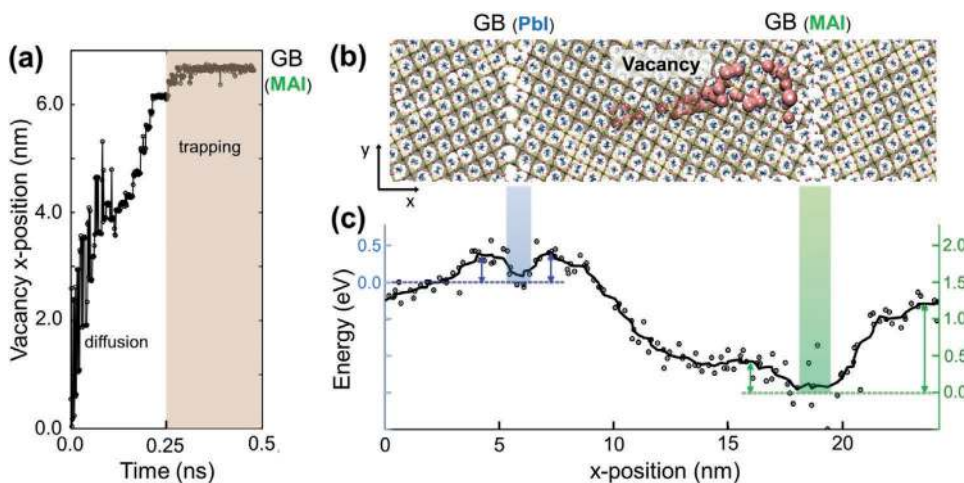


Figure 5. a) The dynamics (x position versus time) of a vacancy in the crystal grain is simulated by molecular dynamics (MD) where it shows that the grain boundaries are able to trap the defects: during the first 0.25 ns of annealing the vacancy diffuses within the grain until it approaches one of the grain boundaries where it remains trapped until the end of the simulation. b) The atomistic structure of the polycrystalline MAPbI_3 model consists of a crystal grain with planar $\Sigma 5/(102)$ boundaries, i.e., PbI-terminated blue and MAI-terminated (green); bubbles represent the vacancy positions during MD. c) Position versus potential energy, obtained by placing the iodine vacancy at different atomic sites (along the dashed line); two local energy minima are found at the boundaries (shaded regions: PbI (blue), MAI (green)) with the lowest one at the MAI-terminated boundary; the energy barriers for the release of defects are also indicated by arrows.

jumps induced by temperature. Accordingly, the mean square displacement increases with time and the defect reaches the GB after 0.25 ns, at a distance of ~6 nm from the initial position. Hereafter, the distance of the defect from the boundary remains (essentially) constant until the end of the simulation, indicating a trapping of the defect at the GB. These findings provide theoretical evidence that GBs can trap defects, thus reducing the overall diffusivity of iodide defects in polycrystalline films.

The physical origin of the trapping can be explained in energetic terms. Grain boundaries are regions of extended defects, typically presenting a local disorder (e.g., coordination defects, strain, etc.) with a corresponding excess of local energy. Accordingly, the energy of a defect at a GB is lower than in the bulk of the crystalline grain. This is confirmed by the potential energy of the vacancy as a function of the position along the polycrystalline system reported in Figure 5c, bottom panel. In practice, we compute the potential energy of the system in which we placed an iodine vacancy at different positions along the x direction of the polycrystalline sample after a local relaxation (dashed line in Figure 5b). The energy profile shows local minima at both GBs (PbI-terminated (blue) and MAI-terminated (green)), indicating that these positions are energetically favored with respect to bulk crystalline regions. In order for the defect to escape from the boundaries it is necessary to overcome an energy barrier $\Delta E^\ddagger \approx 0.5$ eV (1 eV) for the PbI-terminated (MAI-terminated) boundaries. This result is in agreement with the finite temperature dynamics discussed above during which the vacancy is easily captured at the MAI-terminated boundary and never released on the timescale of the simulation.

Present experimental and MD results bring us to the following conceptual scheme: i) When the film is excited by the laser, the defect concentration (V_I , I_i and possibly the corresponding MA defects) increases (Figure 1). ii) Defects can migrate toward and get trapped by the absolute energy minimum (MAI-terminated GB), or toward the local minimum (PbI-terminated GB) because of Brownian-like random dynamics, in which defects jump from site to site due to thermal fluctuations (Figure 5a,b). A net force associated with the energy profile shown in Figure 5c makes the random jumps asymmetric, which result in a net attraction toward the grain boundaries, where they get trapped. iii) When the perturbation, here the focused laser, ceases its action, the system tends to restore the equilibrium defect concentration by annihilating the excess defects (see Figure 4). iv) This requires that complementary defects get detrapped from the grain boundaries, meet and annihilate. In other words, the recovery time is determined by the detrapping time, which, following the transition state theory,^[10,13,54] depends exponentially on the barrier $\tau = \hbar/k_B T \exp[\Delta E^\ddagger/k_B T]$, with \hbar Planck constant, k_B Boltzmann constant, and T temperature. Thus, a recovery time of minutes/hours, as experimentally observed in Figure 4, corresponds to a barrier of $\approx 0.9/1.1$ eV, which is similar to the predictions drawn from the herein shown MD simulations.

3. Conclusion

In this study, we relate signatures of ion migration to the microstructure of MAPbI₃ and studied the effects, as well as kinetics,

of ionic defect migration by PL microscopy. By analyzing the lateral evolution of PL intensity in thin films and single crystals induced by a focused excitation beam, we conclude that grain boundaries inhibit ion movement. The change in PL yield stems from migrating iodide and possibly methylammonium ions that are likely to saturate corresponding vacancies. At the same time, the PL yield reduction comes from the removal of ions from their crystalline sites, which introduces nonradiative recombination centers. This reduction can last for minutes and hours; however, this process can be partially or fully reversible depending on the microstructure. The recovery of PL confirms the possibility of defects being trapped at GBs proximity, which can migrate back to defective crystalline sites to “heal” the lattice upon cessation of the excitation. The experimental findings are supported by molecular dynamics simulations, confirming the trapping of the iodine vacancy at the grain boundaries. The trapping is explained by the presence of potential energy minima for defects at the grain boundaries. The slow recovery process in the dark can be explained by the presence of energy barriers that defects have to overcome in order to detrapp from GBs, after which they can migrate in the crystalline bulk of the grain to encounter the complementary defect and annihilate. We expect that our findings will also help explain the issues faced with long term stability of perovskite solar cells since mobile ionic defects have been shown to play a vital role in degradation mechanisms.^[31]

4. Experimental Section

Samples Fabrication: The glass substrates were cleaned with Mucosal (2%), acetone, and isopropanol in ultrasonicator for 15 min, respectively. Then the substrates were dried with N₂ gun and cleaned in an UV-O₃ cleaner for another 15 min. The cleaned substrates were immediately transferred to a glovebox (N₂ atmosphere) to fabricate the perovskite thin films. The perovskite solutions were made of stoichiometric PbI₂ (Tokyo Chemical Industry, 98% purity) and CH₃NH₃I (Dyename, 99% purity) in a mixed solvent ratio 6:1 of *N,N*-dimethylformamide (Sigma Aldrich, anhydrous, 99.8%) and dimethyl sulfoxide (Sigma Aldrich, anhydrous, 99.8%). To make the big-grain films, 2% of PbI₂ was replaced by Pb(SCN)₂. The solution was shaken at 60 °C for 5 min to dissolve all components. 100 μ L of perovskite solution was dropped on cleaned substrates, then the following spin coating program was used: 20 s at 4000 rpm with ramping steps for 2 s to 1000 rpm then 3 s to 4000 rpm. 5 s before the end of the program, 500 μ L ethyl acetate (Sigma Aldrich, anhydrous, 99.8%) was dropped on the substrates to form a compact film. Immediately after the spin coating, wet perovskite films were annealed at 100 °C for 1 h. To make the crystal, stoichiometry PbI₂ (Tokyo Chemical Industry, 98% purity) and CH₃NH₃I (Dyename, 99% purity) were dissolved in γ -butyrolactone (ReagentPlus, $\geq 99\%$). Subsequently, the solution was heated to 150 °C for 3–8 h to form crystals. The inverted crystallization method to grow crystal was adopted from Saidaminov et al.^[34] All the chemicals were used as received.

Solar Cell Fabrication: The ITO (In-doped SnO₂) substrates were cleaned with the same procedure as above. The cleaned ITO substrates were then coated with SnCl₂ (2 mg mL⁻¹ in ethanol) by using 4000 rpm for 30 s spin coating program. The wet layers were annealed at 180 °C for 1 h. Then the substrates were transferred to N₂ filled glovebox to deposit perovskite layer as mentioned above. Notably, to make small grain devices, the perovskite layer was annealed at 60 °C for 10 min then 50 min at 100 °C whereas big grain devices were annealed at 140 °C in first step. Following the perovskite layer, Spiro-OMETAD was used as hole selective layer in which 36.15 mg of Spiro-OMETAD was dissolved in 1 mL of chlorobenzene, doped with 14.40 μ L 4-*tert*-butylpyridine (Sigma Aldrich, 98%), 8.75 μ L of bis(trifluoromethane)sulfonimide lithium salt (Li-TFSI) (99.95% trace metals basis, Sigma Aldrich) (300 mg mL⁻¹ of acetonitrile),

and 14.50 μL FK209 (Co(II) salt, Sigma Aldrich) (500 mg mL^{-1} of acetonitrile). Finally, 80 nm of Au (Alfa Aesar, 99.99% purity) was evaporated on top at less than 1 \AA s^{-1} rate to finish the device.

Photoluminescence Spectroscopy: A schematic of the photoluminescence spectroscopy setup is shown in Figure S1 (Supporting Information). The measurement was performed in a homebuilt inverted microscope based on the Olympus IX-71 body. For excitation, the 458 nm line of a CW Argon laser was employed. The only exception is for Figure 1 in which we used a 450 nm diode laser (Thorlabs CPS450). The excitation was either focused or collimated at the back aperture of the objective (Olympus LUCPlanFL 40, NA 0.6) with the use of a collimating lens where the former yielded a wide-field excitation spot (“defocused mode”) and the latter yielded a focused spot (“focused mode”). All the data shown in the study were obtained from measurements which were carried out in ambient conditions. In the Supporting Information similar phenomenon of redistribution of PL was demonstrated in space for a single crystal (see Video S2 in the Supporting Information for measurement in air and Video S4 in the Supporting Information for measurement in N_2).

Time-resolved photoluminescence (trPL) measurements were carried out in a home-built setup with an excitation wavelength of 660 nm from a pulsed supercontinuum laser light source (SuperK Extreme) operating at 304 kHz repetition rate. The spot size was 25–35 μm in diameter and the pulse fluence of 10–30 mJ cm^{-2} was chosen in order to generate an equivalent number of charge carriers as would be expected under 1 sun conditions ($1.5 \times 10^{21} \text{ photons m}^{-2} \text{ s}^{-1}$). PL was collected panchromatically and the decay was recorded using time-correlated single photon counting with a PicoHarp TCSPC Module by PicoQuant.

Scanning Electron Microscopic and Energy-Dispersive X-Ray Spectroscopy: The SEM/EDX images were acquired with Hitachi S4100 at 30k magnification. The voltages used for SEM and EDX were 5 and 12.5 keV, respectively.

Classical Molecular Dynamics: The model of a polycrystal with $\Sigma 5/102$ twin boundaries was obtained by i) cutting an orthorhombic crystal of MAPbI_3 with (102) surfaces; ii) generating a replica by a mirror-symmetry about one of the surfaces; iii) merging the two crystals after a relative shift aimed at optimal match of atoms at the boundary; and iv) applying periodic boundary conditions. The 4032-atom model obtained by this procedure was first optimized by conjugate gradient forces minimization, then heated to 300 or 400 K and annealed for 0.3 ns. Vacancy was generated by removal of one iodine atom and its position identified by calculating atomic coordination. The vacancy trajectory and diffusion was studied during 0.5 ns constant number of particles, pressure, and temperature (NPT) dynamics at 400 K and 1 bar.

The energy profile was obtained by i) choosing an atomic configuration equilibrated at 300 K; ii) selecting the iodine atoms along a linear region orthogonal to the boundaries (see Figure 5); iii) placing one vacancy at each of the selected positions; iv) optimizing positions and energy by forces minimization; and iv) collecting all data as a function of position. The profile was obtained by a local running average. All simulations were performed by using the LAMMPS code.^[55]

Supporting Information

Supporting Information is available from the Wiley Online Library or from the author.

Acknowledgements

The authors thank Carola Klimm for acquiring SEM and EDX images. N.P. thanks Dr. Oleksandra Shargaieva and Dr. Qiong Wang for the help with crystal preparation. N.P. thanks the support of Rene Gunder in XRD measurements. N.P. thanks Hans Köbler for the transient measurement support. N.P. acknowledges the Ph.D. program of University of Potsdam. The authors would like to thank Prof. Ivan Scheblykin and Dr. Thomas Unold for providing valuable lab equipment where some of the measurements were made. E.L.U. and A.M. acknowledge funding from the

German Ministry of Education and Research (BMBF) within the program “NanoMatFutur” (Grant No. 03XP0091). A.A.-A. and S.A. acknowledge the BMBF for funding of the Young Investigator Group (Grant No. 03SF0540) within the project “Materialforschung für die Energiewende.” S.M. acknowledges PRACE for awarding him access to Piz Daint CSCS, Switzerland, through projects ADRENALINE (2018184423). A.M. acknowledges Italian MIUR for project PON04a2_00490 M2M Neterg and PRACE for awarding him access to Marconi KNL at CINECA, Italy, through projects UNWRAP (2016153664) and DECONVOLVES (2018184466).

Conflict of Interest

The authors declare no conflict of interest.

Keywords

grain boundaries, halide perovskites, ion migration, molecular dynamic simulations, photoluminescence

Received: November 13, 2019

Revised: January 16, 2020

Published online: April 19, 2020

- [1] M. Saliba, T. Matsui, J.-Y. Seo, K. Domanski, J.-P. Correa-Baena, M. K. Nazeeruddin, S. M. Zakeeruddin, W. Tress, A. Abate, A. Hagfeldt, M. Grätzel, *Energy Environ. Sci.* **2016**, *9*, 1989.
- [2] K. Lin, J. Xing, L. N. Quan, F. P. G. de Arquer, X. Gong, J. Lu, L. Xie, W. Zhao, D. Zhang, C. Yan, W. Li, X. Liu, Y. Lu, J. Kirman, E. H. Sargent, Q. Xiong, Z. Wei, *Nature* **2018**, *562*, 245.
- [3] L. Dou, Y. M. Yang, J. You, Z. Hong, W.-H. Chang, G. Li, Y. Yang, *Nat. Commun.* **2014**, *5*, 5404.
- [4] S. Ahmad, C. George, D. J. Beesley, J. J. Baumberg, M. De Volder, *Nano Lett.* **2018**, *18*, 1856.
- [5] D. Meggiolaro, F. De Angelis, *ACS Energy Lett.* **2018**, *3*, 2206.
- [6] P. Delugas, C. Caddeo, A. Filippetti, A. Mattoni, *J. Phys. Chem. Lett.* **2016**, *7*, 2356.
- [7] C. Eames, J. M. Frost, P. R. Barnes, B. C. O’regan, A. Walsh, M. S. Islam, *Nat. Commun.* **2015**, *6*, 7497.
- [8] C. Zhao, B. Chen, X. Qiao, L. Luan, K. Lu, B. Hu, *Adv. Energy Mater.* **2015**, *5*, 1500279.
- [9] H. J. Snaith, A. Abate, J. M. Ball, G. E. Eperon, T. Leijtens, N. K. Noel, S. D. Stranks, J. T.-W. Wang, K. Wojciechowski, W. Zhang, *J. Phys. Chem. Lett.* **2014**, *5*, 1511.
- [10] S. Meloni, T. Moehl, W. Tress, M. Franckevičius, M. Saliba, Y. H. Lee, P. Gao, M. K. Nazeeruddin, S. M. Zakeeruddin, U. Rothlisberger, M. Graetzel, *Nat. Commun.* **2016**, *7*, 10334.
- [11] K. Domanski, B. Roose, T. Matsui, M. Saliba, S.-H. Turren-Cruz, J.-P. Correa-Baena, C. R. Carmona, G. Richardson, J. M. Foster, F. De Angelis, J. M. Ball, A. Petrozza, N. Mine, M. K. Nazeeruddin, W. Tress, M. Grätzel, U. Steiner, A. Hagfeldt, A. Abate, *Energy Environ. Sci.* **2017**, *10*, 604.
- [12] M. V. Khenkin, K. Anoop, I. Visoly-Fisher, Y. Galagan, F. Di Giacomo, B. R. Patil, G. Sherafatipour, V. Turkovic, H.-G. Rubahn, M. Madsen, T. Merckx, G. Uytterhoeven, J. P. A. Bastos, T. Aernouts, F. Brunetti, M. Lira-Cantu, E. A. Katz, *Energy Environ. Sci.* **2018**, *11*, 739.
- [13] J. M. Azpiroz, E. Mosconi, J. Bisquert, F. De Angelis, *Energy Environ. Sci.* **2015**, *8*, 2118.
- [14] A. Walsh, D. O. Scanlon, S. Chen, X. Gong, S. H. Wei, *Angew. Chem., Int. Ed.* **2015**, *54*, 1791.
- [15] Y. Yuan, J. Chae, Y. Shao, Q. Wang, Z. Xiao, A. Centrone, J. Huang, *Adv. Energy Mater.* **2015**, *5*, 1500615.

- [16] Y. Shao, Y. Fang, T. Li, Q. Wang, Q. Dong, Y. Deng, Y. Yuan, H. Wei, M. Wang, A. Gruverman, J. Shield, J. Huang, *Energy Environ. Sci.* **2016**, *9*, 1752.
- [17] J. S. Yun, J. Seidel, J. Kim, A. M. Soufiani, S. Huang, J. Lau, N. J. Jeon, S. I. Seok, M. A. Green, A. Ho-Baillie, *Adv. Energy Mater.* **2016**, *6*, 1600330.
- [18] J. Xing, Q. Wang, Q. Dong, Y. Yuan, Y. Fang, J. Huang, *Phys. Chem. Chem. Phys.* **2016**, *18*, 30484.
- [19] J. P. Correa-Baena, M. Anaya, G. Lozano, W. Tress, K. Domanski, M. Saliba, T. Matsui, T. J. Jacobsson, M. E. Calvo, A. Abate, M. Grätzel, H. Míguez, A. Hagfeldt, *Adv. Mater.* **2016**, *28*, 5031.
- [20] W. Nie, H. Tsai, R. Asadpour, J.-C. Blancon, A. J. Neukirch, G. Gupta, J. J. Crochet, M. Chhowalla, S. Tretiak, M. A. Alam, H.-L. Wang, A. D. Mohite, *Science* **2015**, *347*, 522.
- [21] C. Caddeo, A. Filippetti, A. Mattoni, *Nano Energy* **2019**, 104162.
- [22] D. W. deQuilettes, W. Zhang, V. M. Burlakov, D. J. Graham, T. Leijtens, A. Osherov, V. Bulović, H. J. Snaith, D. S. Ginger, S. D. Stranks, *Nat. Commun.* **2016**, *7*, 11683.
- [23] C. Li, A. Guerrero, Y. Zhong, A. Gräser, C. A. M. Luna, J. Köhler, J. Bisquert, R. Hildner, S. Huettner, *Small* **2017**, *13*, 1701711.
- [24] S. Chen, X. Wen, S. Huang, F. Huang, Y. B. Cheng, M. Green, A. Ho-Baillie, *Sol. RRL* **2017**, *1*, 1600001.
- [25] A. Merdasa, A. Kiligaridis, C. Rehermann, M. Abdi-Jalebi, J. Stöber, B. Louis, M. Gerhard, S. D. Stranks, E. L. Unger, I. G. Scheblykin, *ACS Energy Lett.* **2019**, *4*, 1370.
- [26] J. F. Galisteo-López, Y. Li, H. Míguez, *J. Phys. Chem. Lett.* **2016**, *7*, 5227.
- [27] J. F. Galisteo-López, M. E. Calvo, H. Míguez, *ACS Appl. Energy Mater.* **2019**, *2*, 6967.
- [28] N. J. Jeon, J. H. Noh, Y. C. Kim, W. S. Yang, S. Ryu, S. I. Seok, *Nat. Mater.* **2014**, *13*, 897.
- [29] U. B. Cappel, S. Svanström, V. Lanzilotto, F. O. Johansson, K. Aitola, B. Philippe, E. Giangrisostomi, R. Ovsyannikov, T. Leitner, A. Föhlisch, S. Svensson, N. Mårtensson, G. Boschloo, A. Lindblad, H. Rensmo, *ACS Appl. Mater. Interfaces* **2017**, *9*, 34970.
- [30] A. Merdasa, M. Bag, Y. Tian, E. Källman, A. Dobrovolsky, I. G. Scheblykin, *J. Phys. Chem. C* **2016**, *120*, 10711.
- [31] S. G. Motti, D. Meggiolaro, S. Martani, R. Sorrentino, A. J. Barker, F. De Angelis, A. Petrozza, *Adv. Mater.* **2019**, *31*, 1901183.
- [32] G. Sadoughi, D. E. Starr, E. Handick, S. D. Stranks, M. Gorgoi, R. G. Wilks, M. Bär, H. J. Snaith, *ACS Appl. Mater. Interfaces* **2015**, *7*, 13440.
- [33] A. Senocrate, I. Moudrakovski, T. Acartürk, R. Merkle, G. Y. Kim, U. Starke, M. Grätzel, J. Maier, *J. Phys. Chem. C* **2018**, *122*, 21803.
- [34] M. I. Saidaminov, A. L. Abdelhady, B. Murali, E. Alarousu, V. M. Burlakov, W. Peng, I. Dursun, L. Wang, Y. He, G. Maculan, A. Goriely, T. Wu, O. F. Mohammed, O. M. Bakr, *Nat. Commun.* **2015**, *6*, 7586.
- [35] S. D. Stranks, G. E. Eperon, G. Grancini, C. Menelaou, M. J. Alcocer, T. Leijtens, L. M. Herz, A. Petrozza, H. J. Snaith, *Science* **2013**, *342*, 341.
- [36] A. Merdasa, Y. Tian, R. Camacho, A. Dobrovolsky, E. Debroye, E. L. Unger, J. Hofkens, V. Sundström, I. G. Scheblykin, *ACS Nano* **2017**, *11*, 5391.
- [37] L. M. Pazos-Outón, M. Szumilo, R. Lamboll, J. M. Richter, M. Crespo-Quesada, M. Abdi-Jalebi, H. J. Beeson, M. Vrućinić, M. Alsari, H. J. Snaith, B. Ehrler, R. H. Friend, F. Deschler, *Science* **2016**, *351*, 1430.
- [38] S. G. Motti, D. Meggiolaro, A. J. Barker, E. Mosconi, C. A. R. Perini, J. M. Ball, M. Gandini, M. Kim, F. De Angelis, A. Petrozza, *Nat. Photonics* **2019**, *13*, 532.
- [39] M. Pazoki, T. J. Jacobsson, J. Kullgren, E. M. Johansson, A. Hagfeldt, G. Boschloo, T. Edvinsson, *ACS Nano* **2017**, *11*, 2823.
- [40] M. Anaya, J. F. Galisteo-López, M. E. Calvo, J. P. Espinós, H. Míguez, *J. Phys. Chem. Lett.* **2018**, *9*, 3891.
- [41] G. W. Adhyaksa, S. Brittman, H. Åboliņš, A. Lof, X. Li, J. D. Keelor, Y. Luo, T. Duevski, R. M. Heeren, S. R. Ellis, D. P. Fenning, E. C. Garnett, *Adv. Mater.* **2018**, *30*, 1804792.
- [42] Y. Kutes, Y. Zhou, J. L. Bosse, J. Steffes, N. P. Padture, B. D. Huey, *Nano Lett.* **2016**, *16*, 3434.
- [43] Y. Tian, M. Peter, E. Unger, M. Abdellah, K. Zheng, T. Pullerits, A. Yartsev, V. Sundström, I. G. Scheblykin, *Phys. Chem. Chem. Phys.* **2015**, *17*, 24978.
- [44] M. Yang, Y. Zeng, Z. Li, D. H. Kim, C.-S. Jiang, J. van de Lagemaat, K. Zhu, *Phys. Chem. Chem. Phys.* **2017**, *19*, 5043.
- [45] N. E. Courtier, J. M. Cave, J. M. Foster, A. B. Walker, G. Richardson, *Energy Environ. Sci.* **2019**, *12*, 396.
- [46] D. R. Ceratti, Y. Rakita, L. Cremonesi, R. Tenne, V. Kalchenko, M. Elbaum, D. Oron, M. A. C. Potenza, G. Hodes, D. Cahen, *Adv. Mater.* **2018**, *30*, 1706273.
- [47] A. Merdasa, S. Tsarev, A. F. Akbulatov, P. Troshin, E. L. Unger, *J. Lumin.* **2019**, 116916.
- [48] Y. Zhong, C. A. M. Luna, R. Hildner, C. Li, S. Huettner, *APL Mater.* **2019**, *7*, 041114.
- [49] A. Mattoni, A. Filippetti, M. Saba, P. Delugas, *J. Phys. Chem. C* **2015**, *119*, 17421.
- [50] A. Mattoni, A. Filippetti, C. Caddeo, *J. Phys.: Condens. Matter* **2016**, *29*, 043001.
- [51] C. Caddeo, C. Melis, M. I. Saba, A. Filippetti, L. Colombo, A. Mattoni, *Phys. Chem. Chem. Phys.* **2016**, *18*, 24318.
- [52] C. Caddeo, M. I. Saba, S. Meloni, A. Filippetti, A. Mattoni, *ACS Nano* **2017**, *11*, 9183.
- [53] R. Long, J. Liu, O. V. Prezhdo, *J. Am. Chem. Soc.* **2016**, *138*, 3884.
- [54] D. G. Truhlar, B. C. Garrett, S. J. Klippenstein, *J. Phys. Chem.* **1996**, *100*, 12771.
- [55] S. Plimpton, *J. Comput. Phys.* **1995**, *117*, 1.